

Mechanical non-reciprocity programmed by shear jamming in soft composite solids

Chang Xu,^{1,*} Shuaihu Wang,^{1,*} Hong Wang,^{2,*} Xu Liu,² Zemin Liu,³ Yiqiu Zhao,^{1,†} Wenqi Hu,^{2,‡} and Qin Xu^{1,§}

¹*Department of Physics, The Hong Kong University of Science and Technology, Hong Kong SAR, China*

²*Department of Mechanical Engineering, The Hong Kong University of Science and Technology, Hong Kong SAR, China*

³*Max Planck Institute for Intelligent Systems, Stuttgart, Germany*

Mechanical non-reciprocity—manifested as asymmetric responses to opposing mechanical stimuli—has traditionally been achieved through intricate structural nonlinearities in metamaterials. However, continuum solids with inherent non-reciprocal mechanics remain underexplored, despite their promising potential for applications such as wave guiding, robotics, and adaptive materials. Here, we introduce a design principle by employing the shear jamming transition from granular physics to engineer non-reciprocal mechanics in soft composite solids. Through the control of the interplay between inclusion contact networks and matrix elasticity, we achieve tunable, direction-dependent asymmetry in both shear and normal mechanical responses. In addition to static regimes, we demonstrate programmable non-reciprocal dynamics by combining responsive magnetic profiles with the anisotropic characteristics of shear-jammed systems. This strategy enables asymmetric spatiotemporal control over motion transmission, a previously challenging feat in soft materials. Our work establishes a novel paradigm for designing non-reciprocal matter, bridging granular physics with soft material engineering to realize functionalities essential for mechano-intelligent systems.

Reciprocity is a fundamental principle in nature, ensuring the symmetric transfer of physical signals in response to stimuli applied from opposite directions [1–3]. Breaking this symmetry through spatiotemporal modulation leads to non-reciprocal dynamics, a phenomenon observed in diverse physical systems such as photonic and phononic circuits [4, 5], quantum-limited amplifiers [6, 7], and acoustic metamaterials [8]. In mechanical systems, these non-reciprocal dynamics enable innovative engineering applications, including enhanced energy harvesting [9, 10], improved shock absorption [11], and the development of mechanical computing technologies [12].

Beyond non-reciprocity in dynamic systems, static non-reciprocity allows for direction-dependent mechanical responses in time-invariant systems [13, 14]. For a static non-reciprocal material, opposite strains ($\pm\gamma$) result in asymmetric shear stresses $\sigma_t(\gamma) \neq \sigma_t(-\gamma)$, or normal stresses $\sigma_n(\gamma) \neq \sigma_n(-\gamma)$, as illustrated in Fig. 1(a). These characteristics are often achieved through the design of mechanical and structural nonlinearities in topological metamaterials. For example, researchers have investigated fishbone structures that violate Maxwell-Betti reciprocity [15] and cylindrical lattices that break the symmetry of normal stress responses [14]. In contrast, mechanical non-reciprocity in continuum solids remains less explored, with Wang *et al.* recently reporting a hydrogel-based composite that exhibits an asymmetric response to shear [16]. From a materials science perspective, non-reciprocity in continuum media is desirable as it does not depend on system size and geometry. However, our understanding of how to design and program this property remains limited.

In this work, we leverage the concept of shear jamming from granular physics [17, 18] to establish a design framework for soft continuum composites with non-reciprocal mechanics. The degree of non-reciprocity arises from

a delicate balance between frictional contact networks and matrix elasticity near the jamming phase boundary, which can be captured by a continuum model based on fiber-reinforced composite theory. By integrating modulated magnetic profiles with shear-jammed states, we further demonstrate programmable non-reciprocal locomotion in these systems, offering a pathway for engineering adaptive materials with direction-dependent mechanics.

RESULTS

Soft composites with shear-jammed inclusions

Soft composites were prepared by first dispersing 22 μm polystyrene (PS) micro-spheres into a polydimethylsiloxane (PDMS) melt. The volume fraction of PS spheres (ϕ) was maintained between the shear jamming threshold ($\phi_m = 56\%$) and the static jamming point ($\phi_0 = 69\%$), ensuring that the PS particles could be jammed by shear [19]. With the crosslinkers and catalyst (0.0061 wt%) pre-mixed in the PDMS solution, the PS–PDMS suspension was slowly crosslinked into a PS–PDMS composite solid. By varying the weight ratio of crosslinkers from $k = 0.71\%$ to 1.43%, the shear modulus of the gel matrix was systematically tuned from $G_m = 0.11$ kPa to 1.25 kPa (Figs. S1 and S2).

As illustrated in Fig. 1(b), we implemented a four-step protocol to incorporate a shear-jammed network within the composites. First, a PS–PDMS suspension was loaded into a 25 mm parallel-plate shear cell controlled by a rheometer (MCR 302, Anton Paar). To eliminate residual stresses, an oscillatory shear, $\gamma(t) = \delta\gamma \sin(\omega t)$ with $\delta\gamma = 10\%$ and $\omega = 10$ rad/s, was applied for 20 mins. The smooth interface of the relaxed suspension confirmed a homogeneous, unjammed state. Second, the

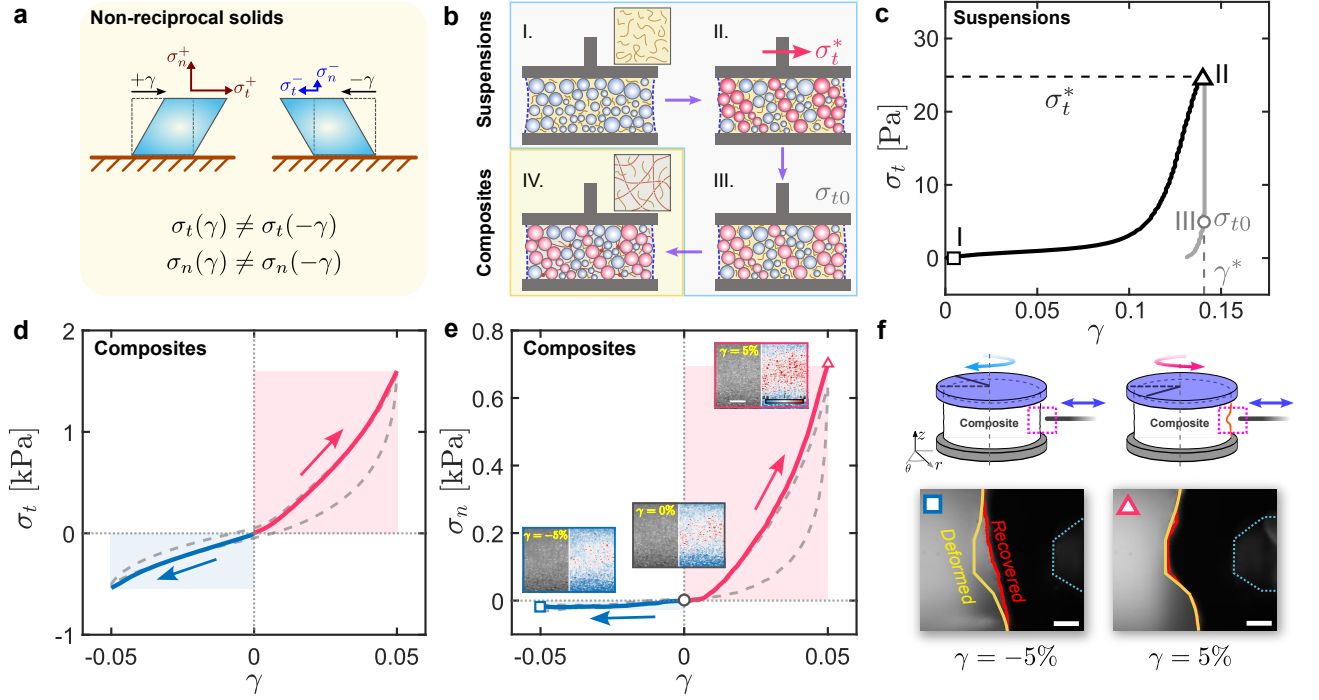


FIG. 1. **Soft composites with non-reciprocal mechanics.** (a) Schematic illustration of materials exhibiting mechanical reciprocity and non-reciprocity. (b) Process of encoding shear-jammed inclusions into soft composites. Steps I to III depict the formation of shear-jammed contact networks during the pre-cured PS-PDMS suspension stages, with the red spheres representing the force-bearing particles. In step IV, the suspension is cured into a composite. (c) Preparation of a jammed network in the pre-cured PS-PDMS suspension. After jamming under a shear strain γ^* , the shear stress decreases from σ_t^* to σ_{t0} while maintaining a constant γ^* . (d) & (e) Asymmetric mechanical responses in shear stress (σ_t) and normal stress (σ_n) as the composites are sheared from undeformed states, respectively. Gray dashed loops indicate the corresponding stress-strain hysteresis. Insets in (e) show both unprocessed (gray) and processed (colored) images of the composite-air interfaces under shear. Scale bar: 200 μm . (f) Asymmetric shape reversibility. At $\gamma = 5\%$, the composite-air interface retains the induced surface deformation, whereas at $\gamma = -5\%$, the interface fully recovers from surface deformation. Scale bar: 250 μm .

shear stress ($\dot{\sigma}_t$) was incrementally increased at a rate of $\dot{\sigma}_t = 0.1 \text{ Pa/s}$. Beyond a critical strain $\gamma_J \approx 11\%$, the stress-strain curve slope ($d\sigma_t/d\gamma$) exhibited a sharp rise (Fig. 1(c)), signaling a rigidity transition via shear jamming. To stabilize the jammed network, the suspension was sheared to a stress σ_t^* under a strain $\gamma^* > \gamma_J$. Third, σ_t was reduced from $\sigma_{t0} = 5 \text{ Pa}$ at a rate of 0.1 Pa/s while maintaining $\gamma = \gamma^*$ (Supplementary Fig. S3). This step minimized the shear stress during subsequent curing process while retaining the particle configurations defined by γ^* . Finally, with $\sigma_t = \sigma_{t0} = 5 \text{ Pa}$, the suspension was cured into a PS-PDMS composite over 12 h. After the completion of crosslinking, σ_t was reduced to zero, establishing the reference state.

Shear jamming controlled non-reciprocity

Figure 1(d) illustrates the asymmetric shear response of a soft composite with $G_m = 0.25 \text{ kPa}$ and $\phi = 63\%$. The PS inclusions were jammed at $\sigma_t^* = 25 \text{ Pa}$ during preparation. Positive shear strain ($\gamma > 0$) is defined as

strain in the same direction as the preparation strain γ^* , while negative strain ($\gamma < 0$) corresponds to the opposite direction. At $\gamma = 0.05$, the composite exhibited a shear stress $\sigma_t = 1600 \text{ Pa}$, approximately three times the magnitude of the stress $\sigma_t = -538 \text{ Pa}$ observed at $\gamma = -0.05$. Unlike conventional non-reciprocal systems [14–16], these shear-jammed composites also displayed asymmetric stress-strain hysteresis. As shown by the dashed grey line in Fig. 1(d), hysteresis is pronounced for $\gamma > 0$ but negligible for $\gamma < 0$.

We attribute these non-reciprocities to the contact configurations encoded in the PS-PDMS suspensions. Previous studies on granular materials demonstrated that shear-jammed networks are anisotropic, with a major axis aligned at approximately 45° relative to the shear direction [20–22]. Within the composites, shear along the jamming direction ($\gamma > 0$) enhances this anisotropy, increasing shear stress and frictional dissipation [17, 23]. Conversely, reverse shear ($\gamma < 0$) softens the contact networks between inclusions, leaving the matrix as the main contributor to shear stress. The reduction in frictional contacts decreases dissipation under quasi-static shear,

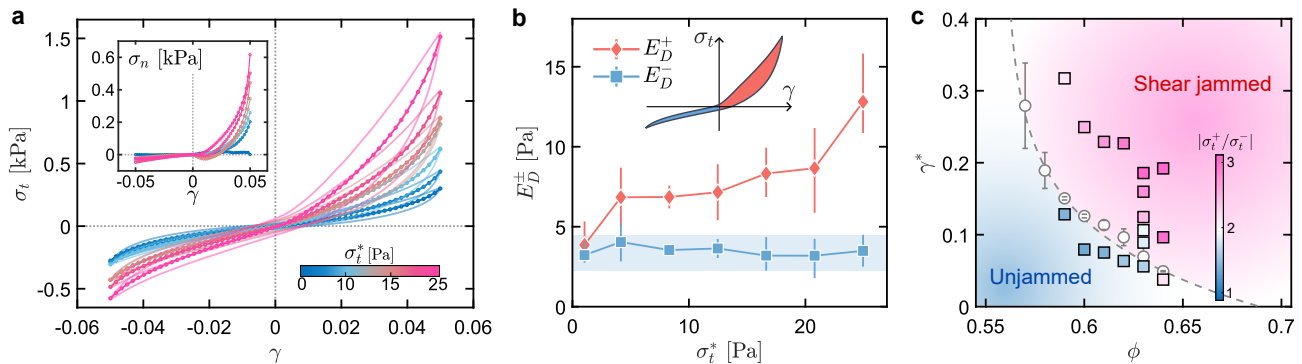


FIG. 2. **Mechanical non-reciprocity controlled by shear jamming transition.** (a) Plots of shear stress (σ_t) against shear strain (γ) for PS-PDMS composites with a constant $\phi = 0.63$ prepared under varying critical shear stresses (σ_t^*) ranging from 1 Pa to 25 Pa. The connected dots represent the mean values of $\sigma_t(\gamma)$ obtained by averaging hysteresis loops at each strain. Inset: plots of associated non-reciprocal normal stress (σ_n) against γ for these composites. (b) Plots of hysteresis loop areas E_D^+ and E_D^- against σ_t^* . (c) Relationship between the shear jamming transition of inclusion and the degree of shear non-reciprocity of the resulting composites. Open circles represent the boundary of shear-jamming transition for PS-PDMS suspensions, fitted to Eq. 1 (dashed line). Squares mark the material parameters (ϕ, γ^*) used to prepare different composite samples, with the filled colors representing the degree of shear non-reciprocity $|\sigma_t^+/\sigma_t^-|$.

resulting in a smaller hysteresis loop for $\gamma < 0$.

The granular characteristics of these soft composites were also evident in their normal stress responses (σ_n). As shown in Fig. 1(e), σ_n remains close to zero for $\gamma < 0$ but increases sharply for $\gamma > 0$, accompanied by a roughening of the composite-air interface (insets in Fig. 1(e)). Similar to frustrated dilation in shear thickened granular suspensions [24, 25], the PS particles tended to protrude at composite-air interfaces for $\gamma > 0$, while being constrained by the PDMS matrix. This dilation tendency under $\gamma > 0$ resulted in pronounced non-reciprocity in σ_n , a phenomenon referred to as asymmetric Poynting effects in solid mechanics [26]. Due to the differences in the governing interaction between $\gamma < 0$ and $\gamma > 0$, the composites also exhibited asymmetric shape reversibility under deformation (Fig. 1(f)). At $\gamma = -0.05$, the surface deformations induced by an external indentation fully recovered after the indenter was removed. In contrast, at $\gamma = 0.05$, the deformed surface profile persisted indefinitely, even in the absence of external forces. This behavior suggests the presence of a shear-controlled switchable memory for surface deformations.

Given that the shear-jammed contact networks formed in the suspension state, we investigated the influence of σ_t^* , which governs shear jamming of inclusions (Fig. 1), on the non-reciprocity in the resulting PS-PDMS composite. Figure 2(a) shows the shear responses of soft composites with constant $G_m = 0.25$ kPa and $\phi = 63\%$, as σ_t^* was varied from 1 to 25 Pa. Here, σ_t^+ and σ_t^- denote the shear stresses measured at $\gamma = 5\%$ and $\gamma = -5\%$, respectively. The degree of shear non-reciprocity, quantified by the ratio $|\sigma_t^+/\sigma_t^-|$, increases with σ_t^* , rising from approximately 1.1 at $\sigma_t^* = 1$ Pa to 3.3 at $\sigma_t^* = 25$ Pa. The non-reciprocal normal responses also exhibited a strong dependence on σ_t^* . As shown in the inset of Fig. 2, τ_n

for $\gamma > 0$ increases with τ_t^* but remains nearly zero for $\gamma < 0$. Finally, the stress-strain hysteresis varied with σ_t^* as well. Using the loop integrals ($E_D^+ = \oint_{\gamma>0} \sigma_t d\gamma$) and ($E_D^- = \oint_{\gamma<0} \sigma_t d\gamma$) to characterize dissipations in the positive and negative shear directions, respectively, we observed that E_D^+ increased substantially with σ_t^* while E_D^- remained nearly constant (Fig. 2 (b)). This further confirmed that σ_t^* controls the contact interactions among PS inclusions for $\gamma > 0$.

The shear-induced non-reciprocal behaviors of PS-PDMS composites were quantitatively connected to shear jamming phase transitions in PS inclusions (Fig. 2(c)). The phase boundary, represented by the open circles, was described by an empirical formula:

$$\phi(\gamma_J) = \phi_m + (\phi_0 - \phi_m)e^{-\gamma_J/\gamma_c} \quad (1)$$

with $\phi_0 = 0.689 \pm 0.004$, $\phi_m = 0.560 \pm 0.002$, and a characteristic strain $\gamma_c = 0.104 \pm 0.003$ (Fig. S4). In addition to mapping the phase boundary, we simultaneously plotted $|\sigma_t^+/\sigma_t^-|$ of soft composites prepared with varying ϕ and γ^* in Fig. 2(c). Below $\phi(\gamma_J)$, $|\sigma_t^+/\sigma_t^-|$ approaches unity, indicating a low degree of shear non-reciprocity. In contrast, this ratio exceeds unity above $\phi(\gamma_J)$ and generally increases with the distance to $\phi(\gamma_J)$.

Besides PS-PDMS composites, we used different particulate inclusions—including glass and poly(methyl methacrylate) (PMMA)—to engineer composites with shear-jammed configurations. Notably, analogous non-reciprocal behaviors were observed across these systems, regardless of inclusion type, underscoring the broad applicability of the proposed design principle (Fig. S5).

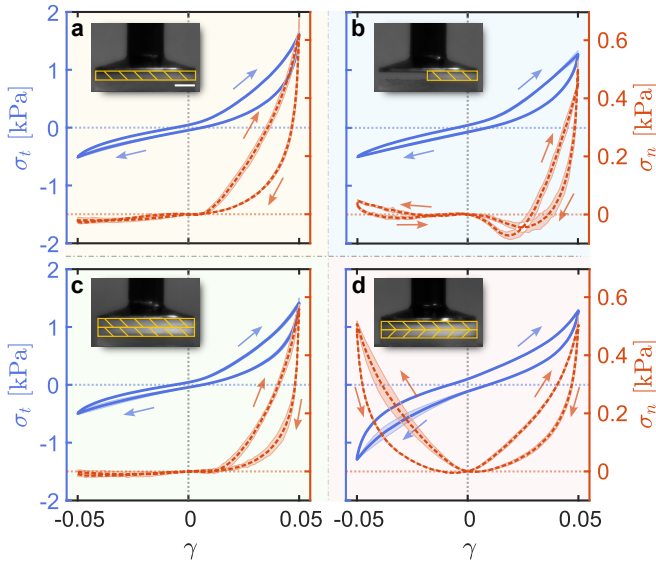


FIG. 3. **Scalable and programmable mechanical non-reciprocity.** (a) Re-plots of non-reciprocal shear stress (σ_t) and normal stress (σ_n) for the composite shown in Figs. 1(d) and (e). Scale bar: 5 mm. (b) Plots of σ_t and σ_n against γ for a half-disk sample cut from the composite shown in (a). (c) Plots of σ_t and σ_n against γ for a two-segment sample created by stacking two composites with force chains aligned in parallel. (d) Plots of σ_t and σ_n against γ for a two-segment sample formed by stacking two composites with force chains aligned perpendicularly.

Scalable and programmable mechanical non-reciprocity

As the bulk of composites remains spatially homogeneous (Fig. S6), the non-reciprocal responses are size independent. Figure 3(a) replots the asymmetric responses of σ_t and σ_n in a soft composite with $G_m = 0.25$ kPa, $\phi = 63\%$, and $\sigma_t^* = 25$ Pa. Cutting this composite in half along its diameter yielded a half-disk sample. As shown in Fig. 3(b), both σ_t and σ_n remain asymmetric against γ , mirroring the responses of a full composite. This demonstrates that the observed mechanical non-reciprocity is an intrinsic, scalable material property.

Furthermore, the shear jamming controlled non-reciprocity enables programmable mechanics in multi-segment composites. As shown in Fig. 3(c), for a two-segment composite with aligned jamming directions, both σ_t and σ_n exhibit the same asymmetric responses to cyclic shear as a single composite. In contrast, a two-segment composite with opposite jamming configurations (Fig. 3(d)) shows symmetric responses against γ , accompanied by enhanced hysteresis for $\gamma < 0$, suggesting that direct particle contacts dominate mechanical responses in both shear directions.

Continuum constitutive model

To elucidate the observed non-reciprocal responses, we develop a continuum constitutive model that treats the composites as fiber-reinforced anisotropic materials [27]. The anisotropic force chains arising from shear jamming are represented as a network of semi-rigid fibers that resist compressive loads but exhibit vanishing rigidity under tension. This framework leads to a strain energy density function, decomposed as $\Psi = \Psi_{\text{vol}} + \Psi_{\text{iso}} + \Psi_{\text{aniso}}$, where $\Psi_{\text{vol}} + \Psi_{\text{iso}}$ accounts for the hyperelastic response of the deformed matrix, while Ψ_{aniso} captures the directional reinforcement contributed by the embedded fibers.

Given a bulk modulus K and a deformation gradient $\mathbf{F} = \partial x / \partial X$, the volumetric strain energy density is

$$\Psi_{\text{vol}} = \frac{K}{2} (J - 1)^2, \quad (2)$$

with $J = \det(\mathbf{F})$. To account for the nonlinear elasticity of the soft silicone matrix under volume-conserving deformations, the isochoric component Ψ_{iso} is characterized by a two-term Yeoh model [28],

$$\Psi_{\text{iso}} = \frac{\mu_1}{2} (\bar{I}_1 - 3) + \frac{\mu_2}{2} (\bar{I}_1 - 3)^2. \quad (3)$$

Here, μ_1 denotes the baseline shear modulus, μ_2 is a material parameter governs nonlinear stiffening, and $\bar{I}_1 = J^{-2/3} I_1$ is the modified first invariant of the Cauchy-Green strain tensor $\mathbf{C} = \mathbf{F}^T \cdot \mathbf{F}$, with $I_1 = \text{Tr}(\mathbf{C})$. The anisotropic contribution from shear-jammed force chains is modeled through a modified Holzapfel-Gasser-Ogden (HGO) formulation [29]

$$\Psi_{\text{ainso}} = \frac{k_1}{2\beta} \left\{ e^{\beta[\kappa \bar{I}_1 + (1-3\kappa)\bar{I}_4 - 1]^2} - 1 \right\} H(1 - \lambda_a), \quad (4)$$

where k_1 (fiber stiffness), κ (fiber dispersion), and β (dimensionless nonlinearity parameter) characterize the composite's directional reinforcement. The pseudo-invariant $\bar{I}_4 = J^{-2/3} I_4$ incorporates the directional stretch $I_4 = \mathbf{a} \cdot \mathbf{C} \mathbf{a}$, with $\mathbf{a} = (-1, 0, 1)/\sqrt{2}$ representing the mean fiber orientation. Critically, the Heaviside function $H(1 - \lambda_a)$ enforces the fibers' semi-rigid response, deactivating their contribution under tension ($\lambda_a = \|\mathbf{F} \mathbf{a}\| \geq 1$).

We directly compared the experimentally measured non-reciprocal σ_t and σ_n with predictions from our constitutive model. To probe the interplay between matrix elasticity and frictional contacts, we varied the matrix shear modulus G_m from 0.11 kPa to 12.5 kPa, while maintaining a constant $\phi = 0.63$ and $\sigma_t^* = 25$ Pa. Figure 4(c) shows the resulting $\sigma_t(\gamma)$ and $\sigma_n(\gamma)$ for composites across this range. For $G_m \leq 2$ kPa, the shear non-reciprocity ratio $|\sigma_t^+ / \sigma_t^-|$ remains nearly constant at ~ 3.3 , but sharply declines to 1.4 for $G_m > 2$ kPa

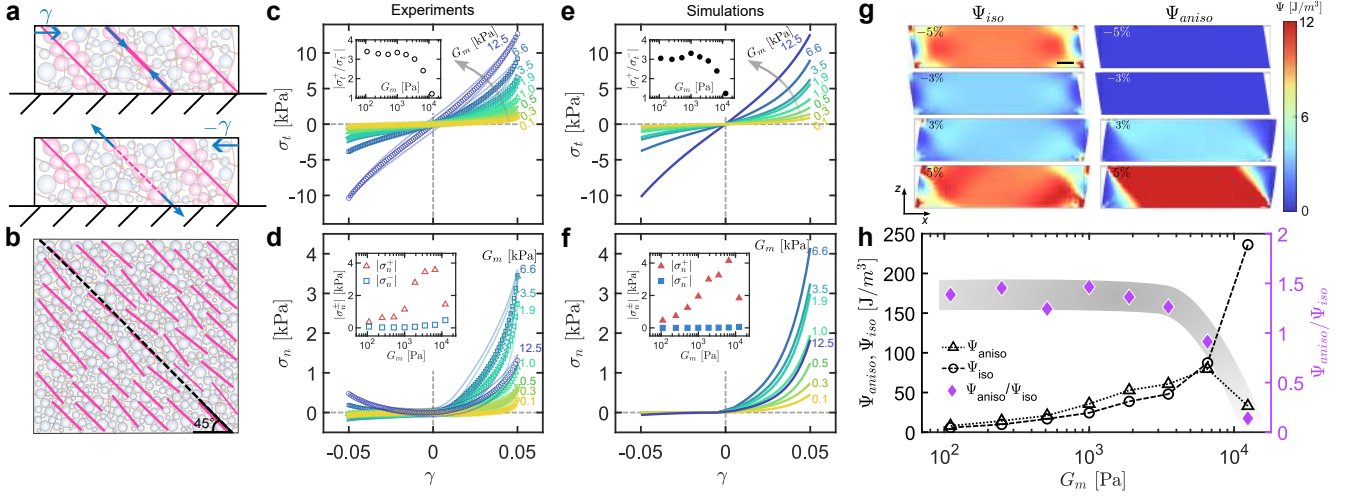


FIG. 4. **Continuum constitutive model.** (a) Modelling of force chains as semi-rigid fibers within composites, which can resist compression (top) but fail under tension (bottom). (b) Schematics of the fiber-reinforced matrix for non-reciprocal composite modelling. Pink lines: fibers in composites dispersed around a mean orientation, approximately 45° to the boundary. (c) & (d) Experimental results of σ_t and σ_n against γ as G_m ranges from 0.1 to 12.1 kPa, and $\phi = 63\%$ and $\sigma_t^* = 25$ Pa remain constant. Inset of (c): experimental results of $|\sigma_t^+/\sigma_t^-|$ versus G_m . Inset of (d): simulation results of σ_n^+ and σ_n^- against G_m , respectively. (e) and (f): Model predictions of σ_t and σ_n against γ , respectively, for different G_m ranging from 0.1 to 12.1 kPa ($\phi = 63\%$ and $\sigma_t^* = 25$ Pa). Inset of (e): simulation results of $|\sigma_t^+/\sigma_t^-|$ versus G_m . Inset of (f): simulation results of σ_t^+ and σ_t^- against G_m , respectively. (g) Distribution of strain energy density (Ψ_{iso} and Ψ_{aniso}) inside a composite ($G_m = 0.25$ kPa, $\phi = 63\%$ and $\sigma_t^* = 25$ Pa) under cyclic shear, derived from the fiber-reinforced model. Scale bar: 2 mm. (h) Left y-axis: plots of Ψ_{iso} and Ψ_{aniso} against G_m . Right y-axis: plot of Ψ_{aniso}/Ψ_{iso} against G_m .

(Fig. 4c, inset), indicating that excessive matrix stiffness reduces shear-jammed contact networks. Additionally, the non-reciprocal normal responses exhibit a distinct dependence on G_m . Analogous to the shear response, we define σ_n^+ and σ_n^- as the normal stresses measured at $\gamma = 5\%$ and -5% , respectively. While $|\sigma_n^-|$ remained insignificant across all tested G_m , $|\sigma_n^+|$ was substantially larger than $|\sigma_n^-|$ and demonstrated a strong dependence on G_m . Notably, $|\sigma_n^+|$ increased from 0.36 kPa to 3.58 kPa as G_m rose from 0.1 kPa to 6.6 kPa, before decreasing to 1.46 kPa at $G_m = 12.5$ kPa. The non-monotonic dependence of both σ_t and σ_n on G_m suggests that moderate matrix elasticity stabilizes force chains, whereas dominant matrix elasticity suppresses force chain efficacy.

Finite element method (FEM) simulations (see Method and Table S1) show that the continuum constitutive model (Eqs. 2 to 4) effectively predicts non-reciprocal σ_t and σ_n for different matrix elasticity (G_m) (Figs. 4(e) and (f)), aligning with the experimental measurements. Figure 4(g) presents the simulated isotropic (Ψ_{iso}) and anisotropic (Ψ_{aniso}) energy densities under cyclic shear for a composite with $G_m = 0.25$ kPa. While Ψ_{iso} remains symmetric with respect to γ , Ψ_{aniso} exhibits pronounced asymmetry between $\gamma > 0$ and $\gamma < 0$, directly leading to non-reciprocal mechanics of composites. To quantify the competition between matrix and force chains, we analyzed Ψ_{iso} and Ψ_{aniso} at $\gamma = 5\%$ across varying G_m in Fig. 4(h). For $G_m \leq 2$ kPa, the ratio Ψ_{aniso}/Ψ_{iso} remains

constant and exceeds unity, confirming the dominance of force chains. Beyond this threshold ($G_m > 2$ kPa), the ratio declines sharply, reflecting the suppression of anisotropic networks in overly rigid matrices. These experimental and computational results collectively confirm that non-reciprocal mechanics emerge from a delicate balance between sufficient matrix compliance to preserve shear-jammed anisotropy and excessive rigidity that disrupts force chain strength.

Non-reciprocal active solids

Beyond static mechanical non-reciprocity, we extended our soft composite design strategy to engineer active solids with non-reciprocal dynamics. To this end, we first prepared a mixture of PS particles and magnetic neodymium iron boron (NdFeB) beads (radius: $5\ \mu\text{m}$) in a PDMS solution, with volume fractions of $\phi_{PS} = 62\%$ and $\phi_{NdFeB} = 1\%$, respectively. The mixture was shear-jammed under a critical stress $\sigma_t^* = 25$ Pa and subsequently cured into a composite with $G_m = 1$ kPa. To program activity, a section of the composite was rolled around a plastic rod (radius: 1.75 mm) and exposed to a 1.2 T magnetic field (Fig. 5(a)). This process encoded a modulated magnetization profile along the material coordinate s , described by:

$$\mathbf{m} = m_0[\cos(\omega_s s + \psi_0), \sin(\omega_s s + \psi_0), 0], \quad (5)$$

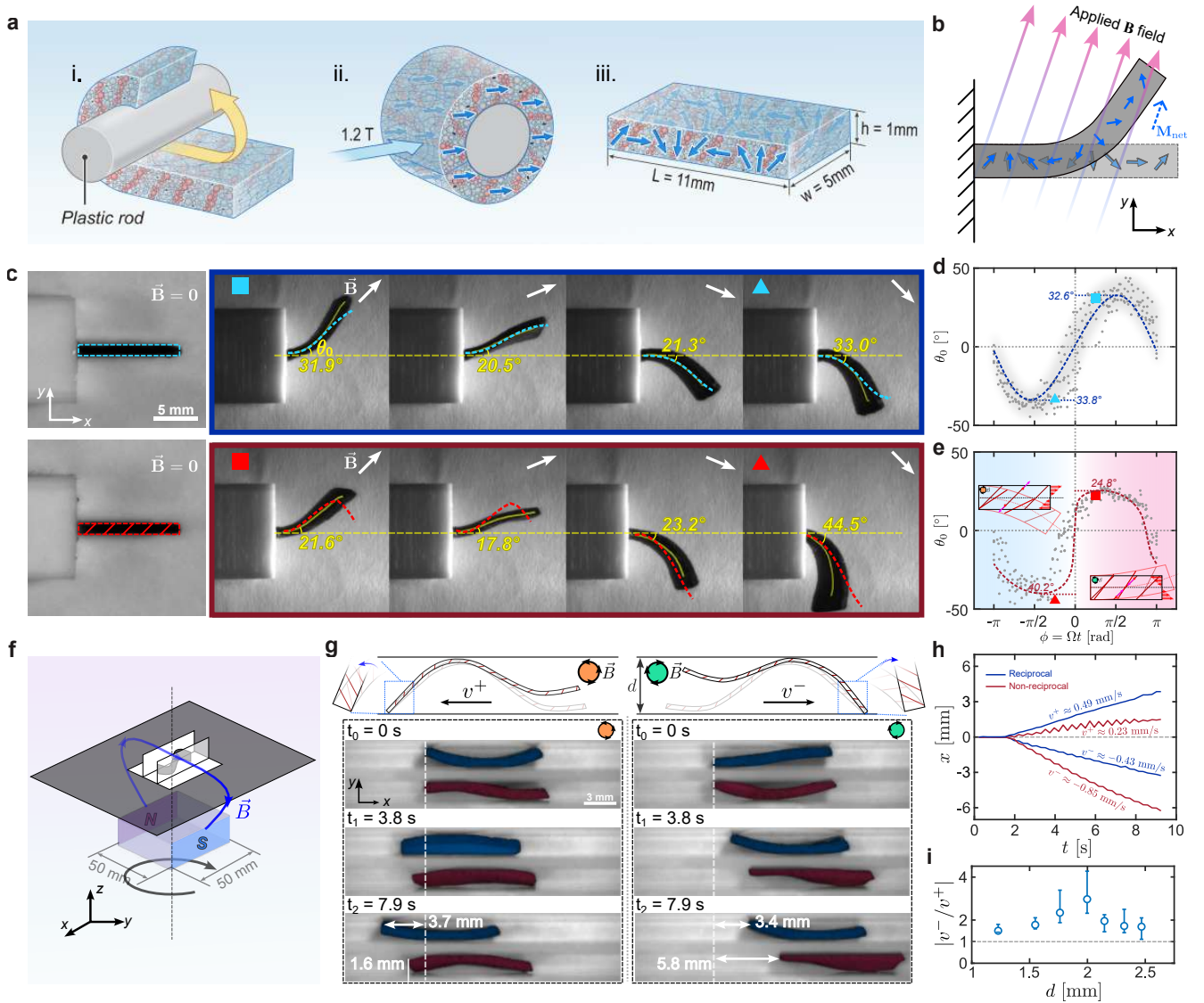


FIG. 5. Non-reciprocal active solids. (a) Fabrication of soft composites incorporating shear-jammed PS inclusions and spatially-modulated magnetic domains. (b) Schematic illustration of a composite sheet bending under a rotational magnetic field \mathbf{B} . (c) Snapshots of an isotropic composite (top: without shear-jammed inclusions) and an anisotropic composite (bottom: with shear-jammed inclusions) bending under a rotational field with $B_0 = 50$ mT and $\Omega = 0.23$ rad/s. Solid yellow lines represent the centerlines of the bending composites, while the colored dashed lines indicate the numerical predictions derived from Eq. 6. (d) Plot of the deflection angle (θ_0) against the orientation of the rotating magnetic field ($\phi = \Omega t$) for the isotropic composite. Gray points represent experimental results and the blue dashed line represents the numerical prediction derived from Eq. 6. (e) Plot of θ_0 against ϕ for the anisotropic composite. Gray points indicate experimental results and the red dashed line shows the numerical prediction obtained by combining the fiber-reinforced model with Eq. 6. Inset: schematic illustration of fibers under compression or tension due to bending. (f) Schematic of the experimental setup where a rotating magnetic (\mathbf{B}) drives the locomotion of sheet-shaped composites in a confined space with gap size d . (g) Depending on the rotational direction of the \mathbf{B} field, a composite can move in either the (+) direction or (-) direction. An isotropic composite (blue) can move in both directions with approximately symmetric speeds ($v^- \approx v^+$), while an anisotropic composite (red) moves substantially faster in the (-) direction than in the (+) direction ($v^- > v^+$). (h) Plots of the horizontal displacement (x) versus time (t) for both reciprocal and non-reciprocal composites. (i) Plot of the ratio $|v^-/v^+|$ against the gap size d .

where m_0 is the magnetization magnitude, ω_s defines the spatial frequency, and ψ represents the initial phase of the magnetization profile.

As shown in Fig. 5(b), the composite sheet exhibits global bending under an external magnetic field due to

its non-zero local magnetization. When subjected to a rotating magnetic field $\mathbf{B} = B_0(\cos \Omega t, \sin \Omega t, 0)$ with $B_0 = 50$ mT, the sheet oscillates in the $x - y$ plane with the same angular frequency Ω . Snapshots in Fig. 5(c) reveal that, for a PS-PDMS composite with unjammed

inclusions ($\sigma_t^* = 0$ Pa), symmetrical bending occurs as \mathbf{B} rotates clockwise with $\Omega = 0.23$ rad/s (top panels). In contrast, a composite with shear jammed inclusions ($\sigma_t^* = 25$ Pa) displays marked bending asymmetry, deflecting downward by a maximum of 44.5° but upward by only 21.6° (bottom panels).

For a composite with a cross-sectional area A , the bending profile results from the local torque balance along the z -direction:

$$-\frac{\partial M_b}{\partial s} = \tau_m A = [A \mathbf{R}_z(\theta)(\mathbf{m} \times \mathbf{B})]_z, \quad (6)$$

where $\mathbf{R}_z(\theta)$ is the rotational matrix in the x - y plane [30, 31]. For reciprocal isotropic composites, $M_b = EI\partial\theta/\partial s$, where E is Young's modulus and I is the area moment of inertia. By solving for $\theta(s)$ using Eq. 6, we derived the profiles of a reciprocal composite sheet under a rotating magnetic field \mathbf{B} , as shown by the blue dashed line in Fig. 5(c). Additionally, the dashed line in Fig. 5(d) plots the predicted deflection angle θ_0 (defined by $\theta|_{s=0}$) against the orientation of \mathbf{B} , $\phi = \Omega t$, demonstrating consistency with the experimental results.

For non-reciprocal composites, however, the elastic torque $\partial M_b/\partial s$ can not be evaluated analytically due to the absence of a direct relationship between M_b and E . To address this, we re-expressed $\partial M_b/\partial s$ as $\theta'(s)\partial M_b/\partial\theta$ (see the Method), which was then numerically evaluated using the fiber-reinforced anisotropic model (Eqs. 2–4). The red dashed lines in Fig. 5(c) represents the theoretically calculated shapes of the non-reciprocal composite, employing the same material parameters as in Fig. 4. A direct comparison between model predictions and experimental measurements is further illustrated by the asymmetric $\theta_0(\phi)$ curves in Fig. 5(e). The fiber-reinforced model also offers a physical interpretation of the observed bending response. Considering a composite with fibers aligned from the top-right to bottom-left (see the insets in Fig. 5(e)), downward bending stretches the fibers, while upward bending compresses them. Due to the inherent asymmetry in the fiber response to stretching versus compression (Eq. 4), the composite exhibits bending asymmetry.

Researchers have explored how soft magnetic materials can mimic biological organisms by exhibiting adaptive locomotion in confined spaces [32]. Here, we demonstrate that encoded shear-jammed structures enable non-reciprocal locomotion in response to confinement. As illustrated in Fig. 5(f), an untethered composite sheet is placed between two acrylic plates with a gap distance $d < 3$ mm. Depending on the rotational direction of the magnetic field (\mathbf{B}), the sheet moves either forward (+) or backward (−). The positive (+) axis corresponds to the direction of pre-shear applied during the shear jamming of the suspensions, while the negative (−) axis denotes the opposite direction.

We prepared two sheet-shaped samples: an isotropic

composite fabricated without pre-shear and an anisotropic composite with shear jammed inclusions formed under $\sigma_t^* = 25$ Pa. Both composites shared identical matrix elasticity ($G_m = 1$ kPa) and ($\phi = 63\%$). Snapshots in Fig. 5(g) directly compare their locomotion dynamics under confinement (gap size $d = 2$ mm) when exposed to a rotating magnetic field (\mathbf{B}) with $B_0 = 50$ mT and $\Omega = 14.3$ rad/s. The isotropic composite (blue) exhibited symmetric motion, displacing approximately ~ 3.5 mm in both directions over 7.9 s. In contrast, the anisotropic composite (red) demonstrated non-reciprocal dynamics, displacing 5.8 mm in the (−) direction but only 1.6 mm in the (+) direction over the same period. Figure 5(h) plots the horizontal displacements $x(t)$ for both composites, showing zig-zag oscillations consistent with a frequency of $\Omega = 14.3$ rad/s. We defined directional velocities $v^+ = x'(t)|_{x>0}$ and $v^- = x'(t)|_{x<0}$ from the mean slopes of these curves. For the anisotropic composite, $v^- \approx -0.85$ mm/s approximately three times $v^+ \approx 0.23$ mm/s, highlighting its directional bias. The degree of dynamic non-reciprocity, quantified by $|v^-/v^+|$, show non-monotonic dependence on the gap size d : increasing d from 1.2 mm to 2.5 mm, $|v^-/v^+|$ first increases, peaked at ~ 3.2 at $d \approx 2$ mm, then decreases (Fig. 5(i) and Fig. S7).

This directional dynamics of the anisotropic sample arises from its asymmetry bending compliance. For the composite in Fig. 5(g), motion depended on anchoring its leading edge to the bottom plate during magnetic field rotation, followed by buckling deformation. Upon release of the leading edge from the bottom plate, the composite advanced stepwise within the confined space [32]. The step frequency matched the magnetic field's rotational frequency (Ω). Anisotropic force chains (Fig. 5(g)) introduced asymmetric buckling: elongation of force chains occurred during motion in the (−) direction, while compression dominated in the (+) direction. This asymmetry amplified bending in the (−) direction, resulting in faster motion ($v^- > v^+$). Under strong confinement ($d < 1.5$ mm), buckling suppression in both directions restored near-symmetric motion ($v_- \approx v_+$). Conversely, in weak confinement ($d \approx 2.5$ mm), unstable anchoring of the leading edge reduced the speed asymmetry ratio $|v_-/v_+|$, as shown in Fig. 5(i).

DISCUSSION AND CONCLUSION

This study introduces a novel paradigm for engineering non-reciprocal soft continuum solids by encoding shear-jammed contact networks during the pre-cured state. By leveraging the intrinsic relationship between shear jamming transitions and the governing interactions in soft composites, we demonstrate how static non-reciprocity – in both shear and normal responses – can be quantitatively

tuned by controlling the proximity to shear-jamming boundary ($\phi(\gamma^*)$) and matrix elasticity (G_m). This mechanics is robustly captured by a continuum constitutive model unifying nonlinear elasticity with semi-rigid fiber mechanics, which elucidates the critical interplay between contact networks and matrix.

In addition to static non-reciprocity, we further show that the shear-jammed configurations synergize with spatially-modulated magnetic domains to achieve programmable non-reciprocal dynamics, enabling a pathway for asymmetric actuation in soft robotic systems. These findings establish a foundational framework based on shear jamming for designing soft materials with highly tailored non-reciprocal functionalities, opening new avenues for advanced engineering applications in energy-efficient actuators and bio-inspired metamaterials.

METHOD

Material preparation — The Polydimethylsiloxane (PDMS) gel matrix was prepared by mixing a silicone base polymer (Gelest, DMS-V31) with a cross-linker copolymer (Gelest, HMS-301) and a Pt-based siloxane complex as catalyst (Gelest, SIP6831.2) [33]. The catalyst concentration was maintained constant at 0.0061%, such that the mixture remained liquid during the first hour and then fully cured within 12 h (Fig. S1). This slow curing process enabled the formation of shear-jammed states in the suspension states. The radius of polystyrene (PS) particles followed a logarithmic normal function $f(r) = \exp[-(\ln(r/r_a))^2/2\sigma]/(\sqrt{2\pi}\sigma r)$ with $r_a = 9.85 \mu\text{m}$ and $\sigma = 0.53$, giving an average $\langle r \rangle = \exp(\ln r_a + \sigma^2/2) = 11.34 \mu\text{m}$. The density of PS particles, measured via sedimentation, is $\rho = 1.047 \pm 0.002 \text{ g/ml}$.

FEM simulation — The FEM simulations of the simple shear (Figs. 4) were conducted using the commercial software COMSOL Multiphysics (COMSOL Inc., Burlington, MA) with the Structural Mechanics Module (Solid Mechanics Interface). The anisotropic constitutive model was implemented via a user-defined strain energy density determined by Eqs. 2–4. For the simple shear configuration, a three-dimensional (3D) rectangular domain (20 mm × 10 mm × 5 mm) was discretized using a swept mesh of hexahedral elements, with a maximum element size of 0.7 mm. Fixed constraints were applied to the bottom boundary, while the top boundary was permitted only horizontal displacement. We applied a horizontal displacement in the range from -0.25 mm to 0.25 mm to the top plate, resulting in a shear strain between -5 % and 5 %. For a deformation gradient \mathbf{F} , the stress-strain relation of composites is expressed as

$$\sigma_{ij} = A_{ijkl}\epsilon_{kl}, \quad (7)$$

with the fourth-order elastic tensor being defined as

$$A_{ijkl} = F_{i\alpha}F_{k\beta} \frac{\partial^2 \Psi}{\partial F_{j\alpha} \partial F_{l\beta}}. \quad (8)$$

Based on Eqs 7 and 8, we calculated the shear stress as $\sigma_t = \sigma_{zx}$ (Fig. 4(e)) and the normal stress as $\sigma_n = \sigma_{zz}$ (Fig. 4(f)). To determine the optimal material parameters, we first identified the elastic pre-factors μ_1 and μ_2 by fitting the simulated to the measured σ_t for $\gamma < 0$, a regime dominated by matrix elasticity. Subsequently, the fiber stiffness k_1 and nonlinear parameter β were determined by fitting the simulated to measured σ_t for $\gamma > 0$, a regime dominated by the shear-jammed inclusions. Given the nearly incompressible nature of PDMS gels, the bulk modulus was set as $K = 100\mu_1$. To approximate the slight alignment dispersion of such systems, we maintained a standard $\kappa = 1/12$ [34] in all our simulations. Within the selected range of material parameters, the simulation results appeared to be insensitive to K and κ . The detailed material parameters are presented in Supplementary Table 1.

Numerical analysis of bending profiles — Considering a local deflection angle θ in the bended composite, the rotational matrix $\mathbf{R}_z(\theta)$ is given by

$$\mathbf{R}_z(\theta) = \begin{bmatrix} \cos \theta & -\sin \theta & 0 \\ \sin \theta & \cos \theta & 0 \\ 0 & 0 & 1 \end{bmatrix}.$$

Consequently, Eq. 6 can be explicitly expressed as

$$\begin{aligned} \partial M_b / \partial s = & \\ & - AB_0 m_0 \{ [\sin(\Omega t) \cos(\omega_s s + \psi_0) - \\ & \cos(\Omega t) \sin(\omega_s s + \psi_0)] \cos(\theta) - \\ & [\sin(\Omega t) \sin(\omega_s s + \psi_0) + \\ & \cos(\Omega t) \cos(\omega_s s + \psi_0)] \sin(\theta) \}. \end{aligned} \quad (9)$$

For the reciprocal composites, we have $\partial M_b / \partial s = EI \partial^2 \theta / \partial s^2$. Thus, a direct integration of Eq. 9 yielded $\theta(s)$, which determines the bending profiles of reciprocal composites. By comparing the experimental profile and theoretically obtained $\theta(s)$ at $t = 0$, we fitted the optimal ϕ_0 and $C_1 = -AB_0 m_0 / EI$. Bending profiles at any given time $t > 0$ were subsequently calculated as shown in Figs. 5(c) and (d).

For the non-reciprocal composites, we considered $\partial M_b / \partial s = \theta'(s) \partial M_b / \partial \theta$, where the term $\partial M_b / \partial \theta$ was calculated using FEM simulations. To align with the experimental geometry in Fig. 5, a computational unit domain (1 mm × 5 mm × 1 mm) with a swept mesh grid (maximum element size: 0.275 mm) was defined. While the left boundary was fixed, we applied a vertical displacement ranging from -0.33 mm to 0.33 mm to the right boundary, and measured the bending momentum

M_b for different deflection angles θ . Using the simulated $\partial M_b / \partial \theta$ along with the fitted ϕ_0 and $C_2 = (-AB_0 m_0)$, we further obtained $\theta(s)$ and bending profiles of the non-reciprocal composites, as shown in Figs. 5(c) and (e).

ACKNOWLEDGEMENTS

We thank Lucio Isa, Ryohei Seto, and Mingcheng Yang for the insightful discussions. This work was supported by the General Research Fund (No. 16307422) and the Collaborative Research Fund (No. C6004-22Y) from the Hong Kong Research Grants Council (RGC). We also appreciate the support of HKUST Marine Robotics and Blue Economy Technology Grant (No. MRBET-002). Yiqiu Zhao acknowledges the support from the RGC postdoctoral fellowship (No. PDFS2324-6S02).

* These authors contributed equally

† yiquizhao@ust.hk

‡ wenqi@ust.hk

§ qinxu@ust.hk

- [1] J. C. Maxwell, L. on the calculation of the equilibrium and stiffness of frames, *The London, Edinburgh, and Dublin Philosophical Magazine and Journal of Science* **27**, 294 (1864).
- [2] H. B. G. Casimir, On onsager's principle of microscopic reversibility, *Rev. Mod. Phys.* **17**, 343 (1945).
- [3] T. Charlton, A historical note on the reciprocal theorem and theory of statically indeterminate frameworks, *Nature* **187**, 231 (1960).
- [4] L. Feng, M. Ayache, J. Huang, Y.-L. Xu, M.-H. Lu, Y.-F. Chen, Y. Fainman, and A. Scherer, Nonreciprocal light propagation in a silicon photonic circuit, *Science* **333**, 729 (2011).
- [5] Y. Wang, B. Yousefzadeh, H. Chen, H. Nassar, G. Huang, and C. Daraio, Observation of nonreciprocal wave propagation in a dynamic phononic lattice, *Physical review letters* **121**, 194301 (2018).
- [6] V. Peano, M. Houde, F. Marquardt, and A. A. Clerk, Topological quantum fluctuations and traveling wave amplifiers, *Physical Review X* **6**, 041026 (2016).
- [7] D. Malz, L. D. Tóth, N. R. Bernier, A. K. Feofanov, T. J. Kippenberg, and A. Nunnenkamp, Quantum-limited directional amplifiers with optomechanics, *Physical review letters* **120**, 023601 (2018).
- [8] Y. Chen, X. Li, H. Nassar, A. N. Norris, C. Daraio, and G. Huang, Nonreciprocal wave propagation in a continuum-based metamaterial with space-time modulated resonators, *Phys. Rev. Appl.* **11**, 064052 (2019).
- [9] J. R. Raney, N. Nadkarni, C. Daraio, D. M. Kochmann, J. A. Lewis, and K. Bertoldi, Stable propagation of mechanical signals in soft media using stored elastic energy, *Proceedings of the National Academy of Sciences* **113**, 9722 (2016).
- [10] M. Hwang and A. F. Arrieta, Input-independent energy harvesting in bistable lattices from transition waves, *Scientific reports* **8**, 3630 (2018).
- [11] L. Wang, J. A. I. Martínez, G. Ulliac, B. Wang, V. Laude, and M. Kadic, Non-reciprocal and non-newtonian mechanical metamaterials, *Nature Communications* **14**, 4778 (2023).
- [12] H. Yasuda, P. R. Buskohl, A. Gillman, T. D. Murphey, S. Stepney, R. A. Vaia, and J. R. Raney, Mechanical computing, *Nature* **598**, 39 (2021).
- [13] M. Shaat, Nonreciprocal elasticity and the realization of static and dynamic nonreciprocity, *Scientific Reports* **10**, 21676 (2020).
- [14] L. Dong, K. Zhou, and D. Wang, Programmable nonreciprocal poynting effect enabled by lattice metamaterials, *Science Advances* **10**, ead15774 (2024).
- [15] C. Coulais, D. Sounas, and A. Alu, Static non-reciprocity in mechanical metamaterials, *Nature* **542**, 461 (2017).
- [16] X. Wang, Z. Li, S. Wang, K. Sano, Z. Sun, Z. Shao, A. Takeishi, S. Matsubara, D. Okumura, N. Sakai, *et al.*, Mechanical nonreciprocity in a uniform composite material, *Science* **380**, 192 (2023).
- [17] D. Bi, J. Zhang, B. Chakraborty, and R. P. Behringer, Jamming by shear, *Nature* **480**, 355 (2011).
- [18] D. Pan, Y. Wang, H. Yoshino, J. Zhang, and Y. Jin, A review on shear jamming, *Physics Reports* **1038**, 1 (2023), a review on shear jamming.
- [19] Y. Zhao, H. Hu, Y. Huang, H. Liu, C. Yan, C. Xu, R. Zhang, Y. Wang, and Q. Xu, Elasticity-controlled jamming criticality in soft composite solids, *Nature Communications* **15**, 1691 (2024).
- [20] R. Seto, A. Singh, B. Chakraborty, M. M. Denn, and J. F. Morris, Shear jamming and fragility in dense suspensions, *Granular Matter* **21**, 1 (2019).
- [21] D. Wang, J. Ren, J. A. Dijksman, H. Zheng, and R. P. Behringer, Microscopic origins of shear jamming for 2d frictional grains, *Phys. Rev. Lett.* **120**, 208004 (2018).
- [22] Y. Zhao, J. Barés, H. Zheng, J. E. S. Socolar, and R. P. Behringer, Shear-jammed, fragile, and steady states in homogeneously strained granular materials, *Phys. Rev. Lett.* **123**, 158001 (2019).
- [23] S. Gallier, E. Lemaire, F. Peters, and L. Lobry, Rheology of sheared suspensions of rough frictional particles, *Journal of Fluid Mechanics* **757**, 514 (2014).
- [24] R. Seto and G. G. Giusteri, Normal stress differences in dense suspensions, *Journal of Fluid Mechanics* **857**, 200–215 (2018).
- [25] H. Hu, Y. Zhao, W. Zhao, L. Qiao, and Q. Xu, Nonmonotonic rheology and stress heterogeneity in confined granular suspensions, *Journal of Rheology* **68**, 949 (2024).
- [26] J. H. Poynting, On pressure perpendicular to the shear planes in finite pure shears, and on the lengthening of loaded wires when twisted, *Proceedings of the Royal Society of London. Series A, Containing Papers of a Mathematical and Physical Character* **82**, 546 (1909).
- [27] A. J. M. Spencer and Z. Hashin, Continuum theory of the mechanics of fibre-reinforced composites, *Journal of Applied Mechanics* **53**, 233 (1986).
- [28] O. H. Yeoh, Some forms of the strain energy function for rubber, *Rubber Chemistry and technology* **66**, 754 (1993).
- [29] G. A. Holzapfel, *Nonlinear solid mechanics: a continuum approach for engineering science* (2002).
- [30] G. Z. Lum, Z. Ye, X. Dong, H. Marvi, O. Erin, W. Hu, and M. Sitti, Shape-programmable magnetic soft matter, *Proceedings of the National Academy of Sciences* **113**, E6007 (2016).

- [31] W. Hu, G. Z. Lum, M. Mastrangeli, and M. Sitti, Small-scale soft-bodied robot with multimodal locomotion, *Nature* **554**, 81 (2018).
- [32] Z. Ren, R. Zhang, R. H. Soon, Z. Liu, W. Hu, P. R. Onck, and M. Sitti, Soft-bodied adaptive multimodal locomotion strategies in fluid-filled confined spaces, *Science Advances* **7**, eabh2022 (2021).
- [33] W. Zhao, J. Zhou, H. Hu, C. Xu, and Q. Xu, The role of crosslinking density in surface stress and surface energy of soft solids, *Soft Matter* **18**, 507 (2022).
- [34] Z. Hou, R. J. Okamoto, and P. V. Bayly, Shear wave propagation and estimation of material parameters in a nonlinear, fibrous material, *Journal of biomechanical engineering* **142**, 051010 (2020).